Journal of Power Sources 193 (2009) 684–690

Contents lists available at ScienceDirect

Journal of Power Sources

journal homepage: www.elsevier.com/locate/jpowsour

Channel aspect ratio effect for serpentine proton exchange membrane fuel cell: Role of sub-rib convection

Xiao-Dong Wang[a], Yuan-Yuan Duan[b], Wei-Mon Yan[c], Duu-Jong Lee[d,*], Ay Su[e], Pei-Hung Chi[e]

[a] Department of Thermal Engineering, School of Mechanical Engineering, University of Science and Technology Beijing, Beijing 100083, China
[b] Key Laboratory for Thermal Science and Power Engineering of Ministry of Education, Tsinghua University, Beijing 100084, China
[c] Department of Mechatronic Engineering, Huafan University, Taipei 22305, Taiwan
[d] Department of Chemical Engineering, National Taiwan University, Taipei 106, Taiwan
[e] Department of Mechanical Engineering, Fuel Cell Center, Yuan Ze University, Taoyuan 300, Taiwan

ARTICLE INFO

Article history:
Received 15 February 2009
Received in revised form 13 April 2009
Accepted 15 April 2009
Available online 23 April 2009

Keywords:
Proton exchange membrane fuel cell
Two-phase model
Flow field design
Flow channel aspect ratio

ABSTRACT

A complete three-dimensional, two-phase, non-isothermal model for proton exchange membrane (PEM) fuel cells was used to investigate the effect of the sub-rib convection on the performances for the single and triple serpentine flow fields at various channel aspect ratios and different thermal constraints. The occurrence of sub-rib convection, which is affected by the serpentine flow field, significantly influences the cell performance if the oxygen supply or membrane moisture content was limited. For single serpentine flow field in which sub-rib convection presents under all ribs, changing channel aspect ratio has minimal effects on cell performance since the oxygen supply is sufficient. For triple serpentine flow field or for serpentine cell with poor external heat loss, owing to limited sub-rib convection or to low membrane moisture content, decrease in channel aspect ratio significantly enhances cell performance. Blocking up the sub-rib convection markedly reduces cell performance. Flow field design for PEM fuel cell should take into consideration the effects of sub-rib convection flow on cell performance.

1. Introduction

The proton exchange membrane (PEM) fuel cells are currently regarded as promising energy-conversion devices owing to their high efficiency, low emissions, and quick start-up capability for suitable power supplies for mobile, stationary, and portable devices. Numerous models and numerical simulations have been developed [1–22]. The flow field design in the bipolar plates is one of the key parameters of a PEM fuel cell, which serves as both the current collector and the reactant distributor. The reactants, as well as the products, are transported to and from the cell through flow channels. Flow field configurations, including parallel, serpentine, interdigitated, and other combined versions, have been developed [23–39].

Wang et al. [37] investigated the effects of the number of flow channel bends, number of serpentine loops, and the flow channel width ratio on the cell performance of PEM fuel cells with serpentine flow fields. Yan et al. [38] proposed a serpentine flow field with outlet channels having modified heights or lengths to improve reactant utilization and liquid water removal in proton exchange membrane fuel cells. Wang et al. [39] examined the effect of flow channel aspect ratio and flow channel cross-section area on the cell performance of PEM fuel cells with parallel and interdigitated flow fields. Their results showed that for the parallel flow field design, lower flow channel aspect ratios and flow channel cross-sectional areas improve cell performance while the interdigitated design has an optimal aspect ratio and cross-sectional area.

The sub-rib convection affects the serpentine flow field [34,36,37,41], which significantly alters the reactant transport efficiency to porous gas diffusion layer and catalyst layer, and the removal rate of liquid water out of the cell. No sufficient discussion on the possible role of sub-rib convection for PEM fuel cell performance is available to the authors' best knowledge. This work aims at exploring the role of sub-rib convection on performance of PEM fuel cell with single and triple serpentine flow fields of varying channel aspect ratio. A three-dimensional, two-phase transport model refined from Wang et al. [40] that considers the heat of reaction and environmental loss was utilized as modeling tool.

2. Numerical model

2.1. Flow field design

The cathode electrochemical reactions produce a large amount of liquid water at low operating voltages. If the liquid water is not properly removed and accumulates in the pores of the porous layers, it restricts the oxygen transport to the gas diffusion layer

* Corresponding author. Tel.: +886 2 23625632; fax: +886 2 23623040.
E-mail address: djlee@ntu.edu.tw (D.-J. Lee).

0378-7753/$ – see front matter © 2009 Elsevier B.V. All rights reserved.
doi:10.1016/j.jpowsour.2009.04.019

Nomenclature

C_p	specified heat ($J\,kg^{-1}\,K^{-1}$)
h_{fg}	evaporation latent heat of water ($J\,kg^{-1}\,K^{-1}$)
I	current density ($A\,m^{-2}$)
I	average current density in the fuel cell ($A\,m^{-2}$)
j	transfer current density ($A\,m^{-3}$)
s	volume ratio occupied by liquid water
S_L	source term due to phase change of water
T	temperature (K)
$\vec{u}$	velocity vector ($m\,s^{-1}$)
V_{cell}	operating voltage (V)
x	x-direction coordinate (m)
y	y-direction coordinate (m)
z	z-direction coordinate (m)

Greek letters

ε	porosity
λ	water content in the membrane
λ_{eff}	effective thermal conductivity ($W\,m^{-1}\,K^{-1}$)
λ_s	thermal conductivity of solid matrix ($W\,m^{-1}\,K^{-1}$)
λ_f	thermal conductivity of fluid phase in the pores ($W\,m^{-1}\,K^{-1}$)
ρ	density ($kg\,m^{-3}$)
σ	electric conductivity ($S\,m^{-1}$)

Subscripts

g	gaseous phase
l	liquid phase

and the catalyst layer, thereby reducing the electrochemical reaction rate. In single serpentine flow field (Fig. 1(a)) with high aspect ratio, pressure between two neighboring points in adjacent channels, like points (a) and (b) in Fig. 1(a), can be significantly different. This pressure difference can overcompete the axial pressure drop to yield cross-leakage flow between adjacent channels, referred to as the sub-rib convection. The sub-rib convection in the serpentine flow field effectively removes liquid water [34,36,37,41]. For the triple serpentine flow field shown in Fig. 1(b), the sub-rib convection occurs only under ribs 3, 6, and 9, and does not under the other ribs. Due to different sub-rib convection flow rates thus yielded, the flow channel aspect ratio should markedly affect the cell performance.

The numerical model for the fuel cell used here includes the anode flow channels, anode gas diffusion layer, anode catalyst layer, proton exchange membrane, cathode catalyst layer, cathode gas diffusion layer, and cathode flow channels. Miniature fuel cells with dimensions of 23 mm × 23 mm × 2.745 mm are considered in this investigation. All cells have the same reaction area of 23 mm × 23 mm and the same gas diffusion layer, catalyst layer, and proton exchange membrane thicknesses. The gas diffusion layer is 0.35 mm thick, the catalyst layer is 0.005 mm thick, and the proton exchange membrane is 0.035 mm thick. The anode flow channels in all cells are assumed to be parallel with channel and rib widths of 1 mm since the anode flow channel geometry has little effect on cell performance, while the cathode flow channels are either the single or triple serpentine flow field designs.

Fig. 1 shows schematics of the single and triple flow field designs used in the present study. All the cells included 12 flow channels with 11 ribs on the cathode side all 1 mm wide and with various cathode flow channel heights of 0.75, 1.00, 1.25, 1.50, and 2.00 mm. The ribs were numbered from 1 to 11 for the convenience of analysis as shown in Fig. 1. The operating conditions are the same in all cells for a fair comparison. The fuel cell temperature was assumed to be non-isothermal with the reactants on the anode side being hydrogen and water vapor with a relative humidity of 100%, while the reactants on the cathode side being oxygen, nitrogen, and water vapor with a relative humidity of 100%. The inlet flow rate on the anode side was 150 $cm^3\,min^{-1}$ and the inlet flow rate on the cathode side was 360 $cm^3\,min^{-1}$.

2.2. Governing equations and solution

The two-fluid method used in the present work was refined from that adopted in Wang et al. [40] to incorporate the heat effects using energy equations for entire cells. The model assumes that the system is steady; the inlet reactants are ideal gases; the flow is laminar; and the porous layers such as the diffusion layer, catalyst layer and PEM are isotropic. The model includes continuity, momentum and species equations for gaseous species, liquid water transport equations in the channels, gas diffusion layers, and catalyst layers, water transport equation in the membrane, electron and proton transport equations. The Bulter–Volumer equation was used to describe electrochemical reactions in the catalyst layers. The main governing equations are listed in Appendix A. The source terms (S_i, S_j, and others) and other relevant physicochemical parameters in Eqs. (A1–A7) are listed in Ref. [40].

The energy equations adopted for the present model were listed as follows:

$$\nabla(\varepsilon(1-s)\rho_g\vec{u}_g C_{p,g}T) + \nabla(\varepsilon s\rho_l\vec{u}_l C_{p,l}T) = \nabla(\lambda_{eff}\nabla T) + j\eta + \frac{i^2}{\sigma} + h_{fg}S_L \quad (1)$$

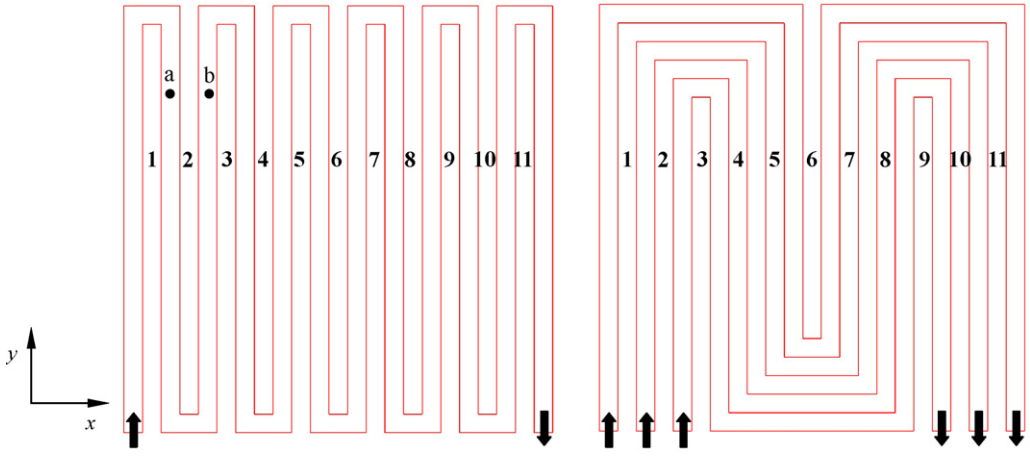

Fig. 1. Schematics of the single and triple serpentine flow fields on the cathode side of the PEM fuel cells: (a) single serpentine and (b) triple serpentine.

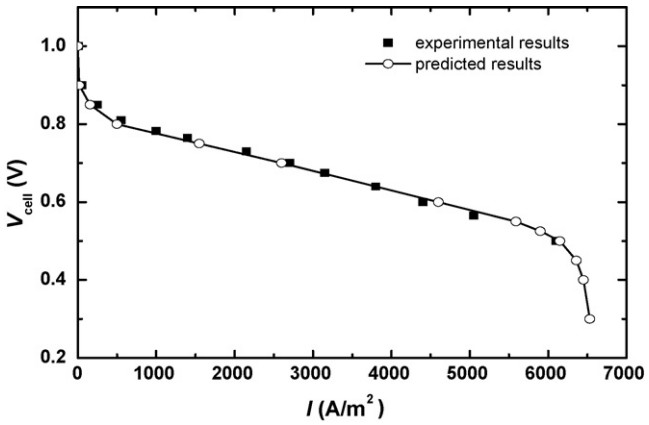

Fig. 2. Comparison of experimental and predicted polarization curves.

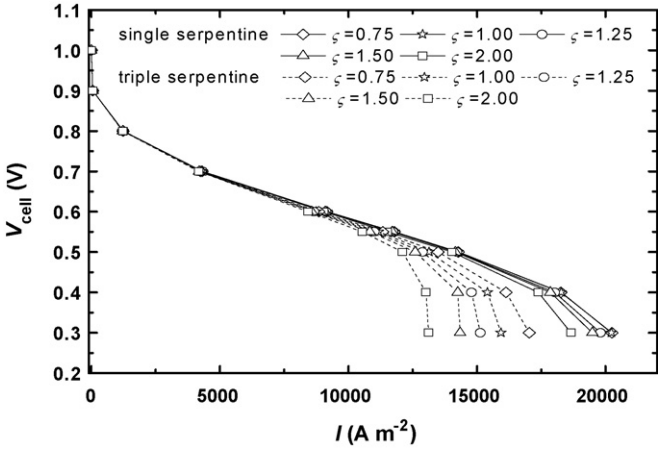

Fig. 3. Polarization curves of single- and triple-PEM fuel cells with various cathode flow channel aspect ratios.

where j is the transfer current density calculated by Bulter–Volumer equation, λ_{eff} is effective thermal conductivity, accounting for the contribution of solid matrix and fluids in the pores of porous media, and can be expressed as

$$\lambda_{eff} = -2\lambda_s + \frac{1}{(\varepsilon/2\lambda_s + \lambda_f) + (1 - \varepsilon/3\lambda_s)} \quad (2)$$

The thermal conductivities of solid matrix were 150 W m^{-1} K^{-1} for the gas diffusion layers, catalyst layers and membrane except otherwise mentioned. The thermal conductivity of the gaseous mixture was obtained by mix kinetic theory and the thermal conductivity of liquid water was considered a function of temperature. The last three terms in Eq. (1) present the electrical work, Joule heating, and latent heat, respectively, owing to water phase change. The other parameters used for calculation were listed in Table 1 of Ref. [40].

The flow rates, compositions and temperatures for anode and cathode channel inlets were constant. No slip boundary conditions were applied to all solid surfaces. The velocities, momentum fluxes, mass fractions and mass fluxes were continuous at interfaces between gas channels, gas diffusion layers, catalyst layers, and the membrane. The surfaces of anode and cathode current collectors are maintained at 323 K or are at a convective condition with heat transfer coefficient, h.

The model used non-uniformly distributed elements with 93, 93 and 33 elements in the x-, y- and z-direction, respectively. The grid independence was examined in preliminary test runs. The non-uniformly distributed grid configuration for the single serpentine PEM fuel cell was composed of 93 × 93 × 33 elements in the x-, y- and z-direction, confirmed in preliminary calculation to accurately describe the cell performance. The numerical results were validated by comparing the present predictions with previous experimental results [42]. Fig. 2 shows that there is only a small difference between the calculated polarization curve and experimental data for a fuel cell with the parallel flow channel design and an area of 141 mm × 141 mm.

3. Results

3.1. Effects of aspect ratio

Fig. 3 shows the polarization curves for the single serpentine flow field and the triple serpentine flow field with various flow channel aspect ratios. At operating voltages higher than 0.7 V, owing to the low electrochemical reaction rate with limited oxygen consumption and water production, all flow designs have the same performance. As the operating voltage decreases, the electrochemical reaction rates increase with increased oxygen consumption and liquid water production. Excessively produced liquid water can block the pores of gas diffusion layer, thereby limiting oxygen transport. Different flow field designs reveal distinct capability to remove water, so as to affect the cell performance. Decrease in aspect ratio in single serpentine flow field improves cell performance (Fig. 3). This noted improvement declines as aspect ratio decreases further down. The flow channel aspect ratio affects more profoundly the cell performance with triple serpentine flow field than that with

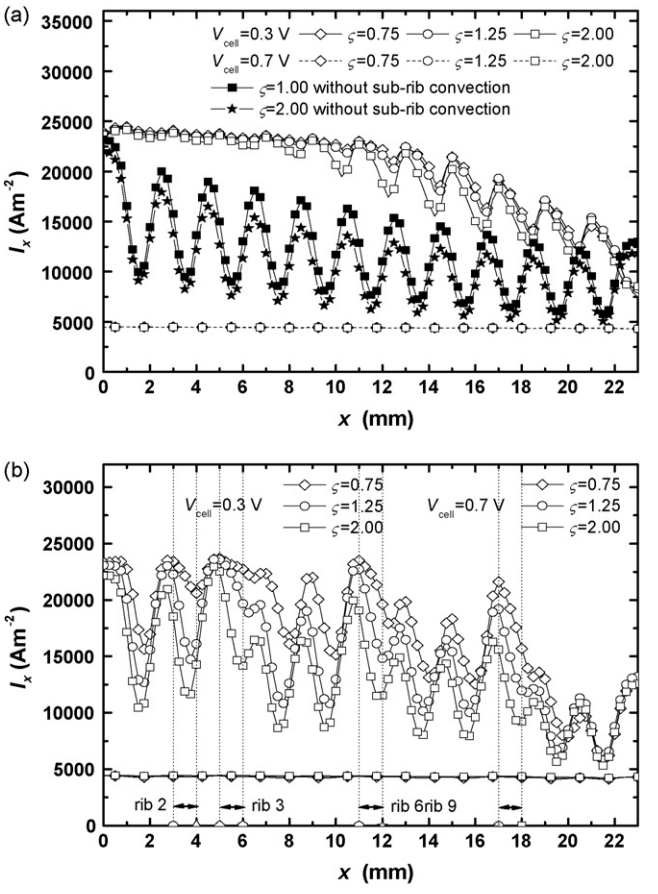

Fig. 4. Local current density distributions at y = 11.5 mm in the middle cross-section in the membrane for various cathode flow channel aspect ratios: (a) single serpentine flow field and (b) triple serpentine flow field.

single flow field. This occurrence was attributable to the strong sub-rib convection presented for the single serpentine flow field (discussed later).

3.2. Local current distributions

The channel aspect ratio has more significant effects on local current density distribution for the triple than the single serpentine flow fields (Fig. 4(a) and (b)). The gas flow rate for single serpentine flow field sufficiently provides oxygen to maintain constant chemical reaction rate in the first half of cell at all channel aspects studied. The oxygen supply is limited for the second half of single serpentine flow cell so the effects of channel aspect ratio are unveiled. The triple serpentine flow cell has low gas flow rate so the channel aspect ratio affects the current density distribution for the entire cell.

3.3. Local liquid water distributions

Fig. 5(a) shows the liquid water distributions at $y = 11.5$ mm on the interface between the cathode gas diffusion layer and the catalyst layer for the single serpentine flow field at different flow channel aspect ratios. At 0.7 V, the liquid water distributions are lower with different aspect ratios. At 0.3 V, the liquid water concentrations are far greater than for at 0.7 V due to the stronger electrochemical reaction rates. Moreover, the liquid water concentration gradually increases with increasing x because the produced liquid water moves to the downstream due to the gas phase shear forces. As the flow channel aspect ratios decreases, the reactant inlet velocity increases with higher shear forces, which help remove the liquid water out of the porous layers; therefore, the liquid water concentrations are reduced. The liquid water content is much higher for triple serpentine flow cell than the single serpentine flow cell (Fig. 5(b)).

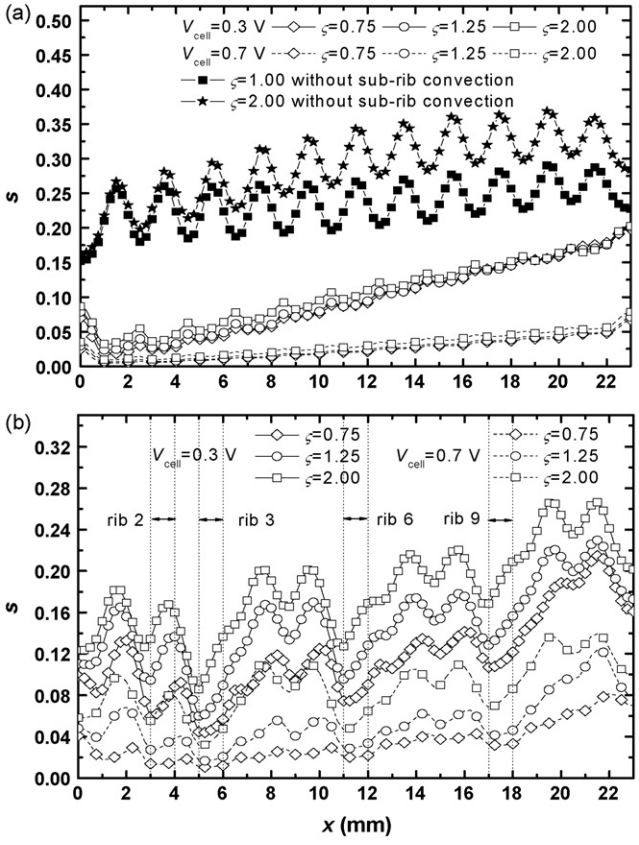

Fig. 5. Liquid water distributions at $y = 11.5$ mm on the cathode gas diffusion layer–catalyst layer interface for various cathode flow channel aspect ratios: (a) single serpentine flow field and (b) triple serpentine flow field.

Table 1
Cathode pressure drops for various flow fields.

ζ (single)	Δp (Pa)	ζ (triple)	Δp (Pa)
2.00	223.4	2.00	66.3
1.50	329.2	1.50	101.85
1.25	383.7	1.25	164.63
1.00	486.5	1.00	234.52
0.75	633.4	0.75	327.21

3.4. Pressure drop

Table 1 shows the pressure drops on the cathode side of the entire cell for the single and triple serpentine flow fields. The cathode pressure drops for the triple serpentine flow field are lower than for the single serpentine flow field. For both designs, the cathode pressure drops increase as the flow channel aspect ratio decreases. When the flow channel aspect ratio decreases from 1.00 to 0.75, the cathode pressure drops increase by 146.9 Pa with almost the same cell performance for the single serpentine flow field and by 92.7 Pa with significantly increased cell performance for the triple serpentine flow field. Therefore, decreasing the flow channel aspect ratio is an effective means for improving cell performance for the triple serpentine flow field. In practical applications, where the serpentine flow has many serpentine loops, the proper flow channel aspect ratio will be crucial.

4. Discussion

4.1. Sub-rib convection in cell

The gas velocities in diffusion layer under ribs 2 and 3, the said sub-rib convection velocities, were much higher for single serpentine flow than the triple serpentine flow cells (Fig. 6). Restated, the single serpentine flow field has much stronger sub-rib convection than the triple serpentine flow field. For example, at aspect ratio of 1.25, the velocity ranges 0.2–0.8 m s^{-1} under ribs 2 and 3 for the single serpentine flow field, while it ranges 0.04–0.07 m s^{-1} under rib 2 and 0.05–0.3 m s^{-1} under rib 3 for the triple serpentine flow field.

The sub-rib convection increases as the channel aspect ratio decreases in the single serpentine flow cell. Sufficient oxygen can be supplied for single flow cell at $\zeta = 2$, so the increase in sub-rib convection does not enhance local current density. For the triple serpentine flow field, the pressure difference between two sides of rib 3 increases at decreased y, hence yielding strong sub-rib convection over rib 3. However, the sub-rib convection does not occur under rib 2. At $\zeta = 2$, the gas velocity is too low (about 0.02 m s^{-1} under rib 2, about 0.02–0.11 m s^{-1} under rib 3) to transport sufficient oxygen to porous electrode. As ζ decreases, the velocities under ribs 2 and 3 all significantly increase. For example, at $\zeta = 0.75$, the velocity ranges 0.07–0.12 m s^{-1} under rib 2 and 0.03–0.5 m s^{-1} under rib 3, which significantly enhances the local current density. Therefore, the occurrence of sub-rib convection, which is affected by the serpentine flow field, significantly influences the cell performance if the oxygen supply is limited. Similar observation is applicable to all other ribs, but the sub-rib convection in the second half of cell becomes weaker owing to consumption of reactant along the flow channel (Fig. 7).

Fig. 8 shows the polarization curves for the single serpentine flow field at $\zeta = 1$ using isothermal and non-isothermal model. The cell performance with non-isothermal model at constant-

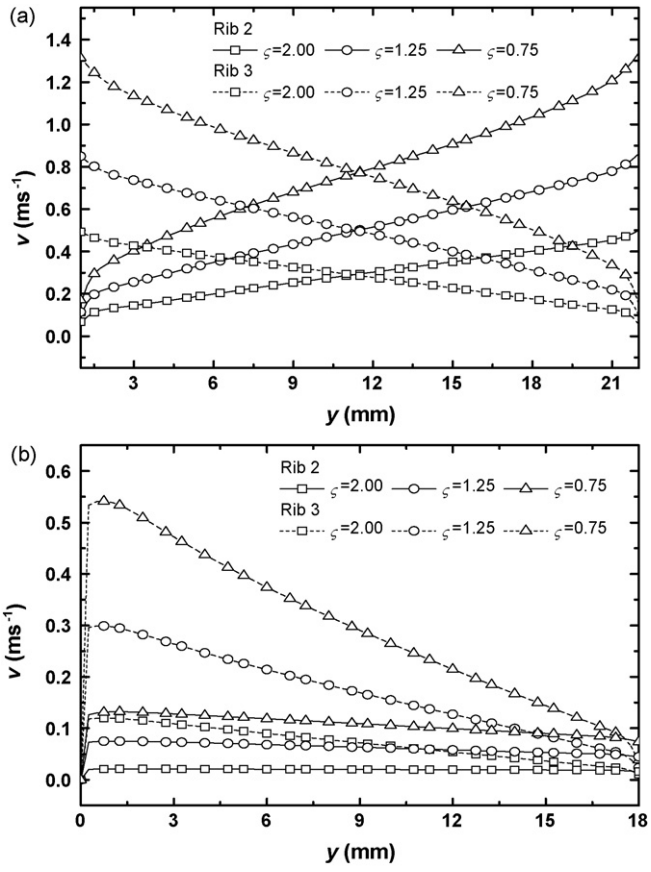

Fig. 6. Velocity distributions of gaseous species under ribs 2 and 3 in the cathode gas diffusion layer: (a) single serpentine and (b) triple serpentine.

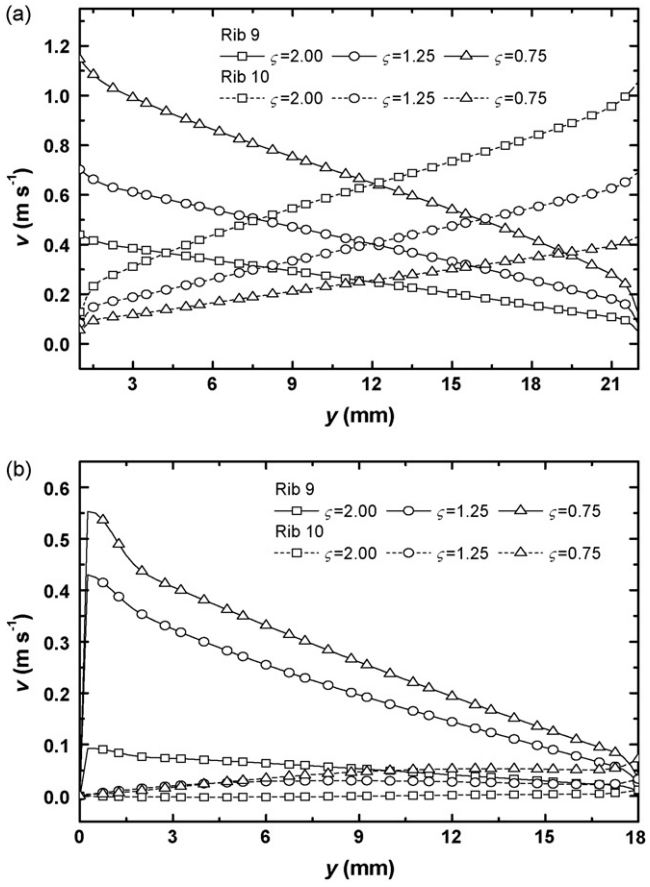

Fig. 7. Velocity distributions of gaseous species under ribs 9 and 10 in the cathode gas diffusion layer: (a) single serpentine and (b) triple serpentine.

temperature surfaces (323 K) and low k values of 0.5 W m^{-1} K^{-1} coincides with those with isothermal model. Effects of h values principally affect the cell performance, while the decreased k values reduced cell performance. Temperature in the cathode gas diffusion layer under rib 3 is shown in Fig. 9. At h = 10 W m^{-2} K^{-1} and k = 0.5 W m^{-1} K^{-1} the cell temperature increased to 364–382 K. Correspondingly, the cell performance becomes poor (Fig. 8). The corresponding sub-rib convection velocity distributions in the diffusion layer and water contents in the membrane under ribs 3 are shown in Figs. 10 and 11. The increase in temperature of the cathode gas diffusion layer results in stronger sub-rib convection (Fig. 10). However, although the oxygen transfer rate is enhanced with strong sub-rib convection, the too high temperature reduces the membrane water content and increases proton transport resistance, which significantly reduces cell performance. Waste heat should be effectively removed from cell to prevent membrane dry-out.

4.2. Role of sub-rib convection and implication to flow field design

For the single serpentine flow field, few difference in the current densities presents under the flow channels and under the ribs (Fig. 4). However, for the triple serpentine flow field, the sub-rib convection occurs only under rib 3 (5 mm < x < 6 mm), rib 6 (11 mm < x < 12 mm), and rib 9 (17 mm < x < 18 mm). For ribs where the sub-rib convection does not occur, for example under rib 2 (3 mm < x < 4 mm), the oxygen transfer rate to the catalyst layer by pure diffusion is much lower than that under the adjacent two flow channels, so producing lower current density.

At 0.3 V the liquid water distributions for the triple serpentine flow field differ markedly from those for the single flow field (Fig. 5(a) and (b)). The sub-rib convection presents under all ribs in single serpentine flow field to enhance liquid water removal. However, for the triple serpentine flow field where the sub-rib convection occurs only under ribs 3, 6, and 9 to lead to low liquid water concentration. However, under rib 2, although it is located near the cell inlet, the liquid water concentrations are still higher than those under ribs 3, 6, and 9 because of lacking sub-rib convection. Impact of reducing channel aspect ratio effectively declines liquid

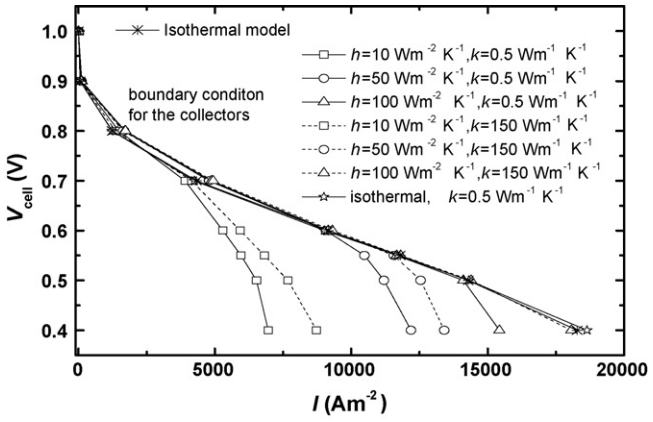

Fig. 8. Polarization curves for the single serpentine flow field with an aspect ratio of 1.00 at various thermal boundary conditions.

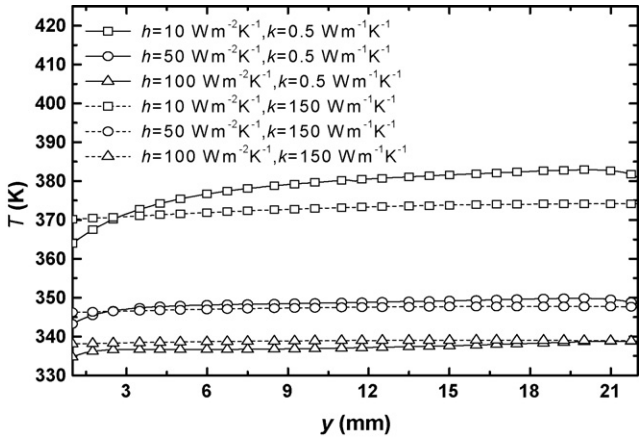

Fig. 9. Temperature distributions in the cathode gas diffusion layer under rib 3 for the single serpentine flow field with an aspect ratio of 1.00 at various thermal boundary conditions.

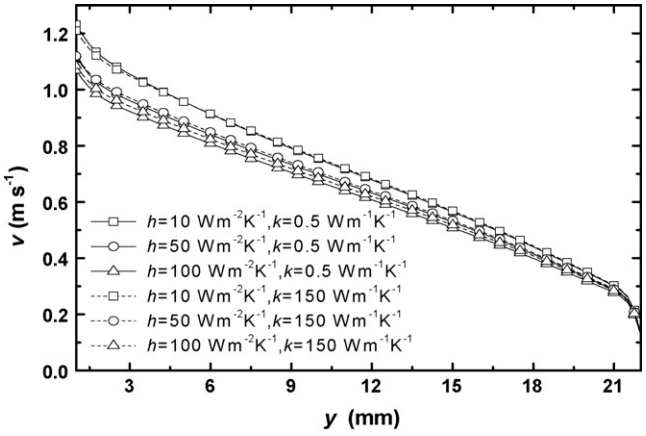

Fig. 10. Velocity distributions of gaseous species under rib 3 in the cathode gas diffusion layer for the single serpentine flow field with an aspect ratio of 1.00 at various thermal boundary conditions.

water concentration in cell for triple serpentine flow field since the corresponding sub-rib convection is weak.

At $\zeta = 1.25$, for instance, the mean velocities in channel between ribs 1 and 2 are 3.40 m s^{-1} and 2.18 m s^{-1} for single and triple serpentine flow fields, respectively. The corresponding mean sub-rib convection flow under rib 2 are 0.49 m s^{-1} and 0.058 m s^{-1},

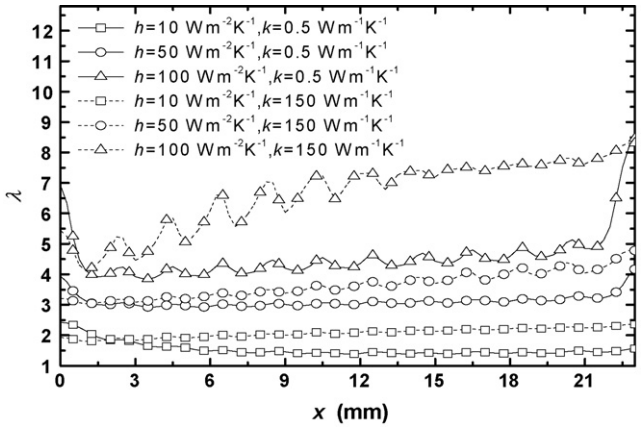

Fig. 11. Water content of membrane along cell width direction for the single serpentine flow field with an aspect ratio of 1.00 at various thermal boundary conditions.

accounting for 14.4% and 2.67% of the corresponding channel velocities, respectively. Meanwhile, the mean velocities in channel between ribs 2 and 3 are 3.30 m s^{-1} and for single and 1.99 m s^{-1} for triple serpentine flow fields. The corresponding mean sub-rib convection flow under rib 3 are 0.48 m s^{-1} and 0.155 m s^{-1}, accounting for 14.5% and 7.78% of the corresponding channel velocities, respectively. Clearly the sub-rib convection can account for a significant part for gas transport in both single and triple serpentine flow fields; with the effects for the former in a stronger and spatially more uniform way than the latter.

A parallel cell simulation was made by setting the middle cross-section along y-direction as impermeable to "switch off" the sub-rib convection. Fig. 4(a) shows that the local current density distribution of the single serpentine flow field without sub-rib convection resembles those of multi-parallel flow field, with local current density periodically varies along the cell width (x-direction). Fig. 5(a) shows the corresponding liquid water distributions. Without sub-rib convection, the liquid water concentration is much higher and the local current density is much lower than those with sub-rib convection. The role of sub-rib convection on cell performance is clearly demonstrated.

The sub-rib convection significantly affects the current densities distribution over the cell, hence the overall performance. Strong sub-rib convection enhances mass transfer efficiency at sub-rib regime and facilitates removal of liquid water from cell. But too strong sub-rib convection requires high pumping works and can lead to low liquid concentration for membrane dry-out. An effective design scheme for flow field should consider the effects of sub-rib convection flow on cell performance.

5. Conclusions

This paper investigated the flow fields, temperature and species distributions in a momentum, heat and mass transfer processes in a PEM fuel cell of dimensions of 23 mm × 23 mm × 2.745 mm. The complete three-dimensional, two-phase, non-isothermal model for PEM fuel cells based on the two-fluid method was numerically solved with constant-temperature or convective boundary conditions at surfaces of anode and cathode current collectors. At operating voltages <0.7 V, the reduced flow channel aspect ratio increases the reactant inlet flow velocity, enhances liquid water removal, and promotes oxygen transport to the porous layers and the cell performance. The sub-rib convection increases as the channel aspect ratio decreases. The sub-rib convection is much higher for single serpentine flow than the triple serpentine flow cells. Reduced external heat transfer coefficients and internal layer thermal conductivities increase intra-cell temperatures, leads to strong sub-rib convection. Too strong sub-rib convection together with high cell temperature may yield membrane dry-out for poor cell performance. The occurrence of sub-rib convection, which is affected by the serpentine flow field, significantly influences the cell performance if the oxygen supply or membrane moisture content were limited. An effective design scheme for flow field should consider the effects of sub-rib convection flow on cell performance.

Acknowledgement

This study was supported by the National Natural Science Foundation of China (No. 50636020 and No. 50876009).

Appendix A

(i) Continuity equation for the gaseous species:

$$\nabla(\varepsilon\rho_g\vec{u}_g) = -S_L \quad \text{(A1)}$$

(i) Momentum equation for the gaseous species:

$$\frac{\varepsilon}{(1-s)^2}\nabla(\rho_g \vec{u}_g \vec{u}_g) = -\varepsilon \nabla p_g + \frac{\varepsilon}{(1-s)}\nabla(\mu_g \nabla \vec{u}_g) + S_{\vec{u}} \quad \text{(A2)}$$

(ii) Species equation for the gaseous species:

$$\nabla(\varepsilon \rho_g \vec{u}_g C_k) = \nabla(\rho_g D_{k,\text{eff}} \nabla C_k) + S_c - S_L \quad \text{(A3)}$$

(iii) Liquid water transport equation in the flow channels, gas diffusion layers and catalyst layers:

$$\nabla\left(\frac{\rho_l k_p k_{rl}}{\mu_l}\frac{\partial p_c}{\partial s}\nabla s\right) - \nabla\left(\frac{\rho_l k_p k_{rl}}{\mu_l}\nabla p_g\right) + \nabla\left(\frac{n_d M_{H_2O}}{F}\vec{i}_m\right) = S_L \quad \text{(A4)}$$

(iv) Liquid water transport equation in the membrane:

$$\nabla\left(\left(\frac{\alpha_d M_{H_2O}}{F}\vec{i}_m\right)\lambda - \left(\frac{M_{H_2O}\rho_{dry}}{M_m}D_\lambda\right)\nabla\lambda\right) = 0 \quad \text{(A5)}$$

(v) Proton and electron transport equations:

$$\nabla(\sigma_m \nabla \Phi_m) = S_j \quad \text{(A6)}$$

$$\nabla(\sigma_s \nabla \Phi_s) = -S_j \quad \text{(A7)}$$

References

[1] T.E. Springer, T.A. Zawodinski, S. Gottesfeld, J. Electrochem. Soc. 136 (1991) 2334.
[2] T.E. Springer, M.S. Wilson, S. Gottesfeld, J. Electrochem. Soc. 140 (1993) 3513.
[3] D.M. Bernardi, M.W. Verbrugge, AIChE J. 37 (1991) 1151.
[4] D.M. Bernardi, M.W. Verbrugge, J. Electrochem. Soc. 139 (1992) 2477.
[5] T.F. Fuller, J. Newman, J. Electrochem. Soc. 140 (1993) 1218.
[6] T.V. Nguyen, R.E. White, J. Electrochem. Soc. 140 (1993) 2178.
[7] V. Gurau, H. Liu, S. Kakac, AIChE J. 44 (1998) 2410.
[8] J.S. Yi, T.V. Nguyen, J. Electrochem. Soc. 145 (1998) 1149.
[9] J.S. Yi, T.V. Nguyen, J. Electrochem. Soc. 146 (1999) 38.
[10] W.B. Gu, C.Y. Wang, B.Y. Liaw, J. Electrochem. Soc. 144 (1997) 2053.
[11] S. Um, C.Y. Wang, J. Electrochem. Soc. 147 (2000) 4485.
[12] T. Berning, D.M. Lu, N. Djilali, J. Power Sources 106 (2002) 284.
[13] A.A. Kulikovsky, J. Electrochem. Soc. 150 (2003) A1432.
[14] S.H. Ge, B.L. Yi, J. Power Sources 124 (2003) 1.
[15] N.P. Siegel, M.W. Ellis, D.J. Nelson, M.R. von Spakovsky, J. Power Sources 132 (2003) 127.
[16] S. Mazumder, J.V. Cole, J. Electrochem. Soc. 150 (2003) A1503.
[17] S. Mazumder, J.V. Cole, J. Electrochem. Soc. 150 (2003) A1510.
[18] W.Q. Tao, C.H. Min, X.L. Liu, Y.L. He, B.H. Yin, W. Jiang, J. Power Sources 160 (2006) 359.
[19] J.J. Hwang, J. Power Sources 164 (2007) 174.
[20] H. Meng, J. Power Sources 168 (2007) 218.
[21] H. Meng, J. Power Sources 164 (2007) 688.
[22] H. Meng, J. Power Sources 162 (2006) 426.
[23] T.V. Nguyen, J. Electrochem. Soc. 143 (1996) L103.
[24] X.D. Wang, Y.Y. Duan, W.M. Yan, J. Power Sources 172 (2007) 265.
[25] H.C. Liu, W.M. Yan, X.D. Wang, J. Electrochem. Soc. 154B (2007) 1338.
[26] S.W. Cha, R. O'Hayre, Y. Satio, F.B. Prinz, J. Power Sources 134 (2004) 57.
[27] H.C. Liu, W.M. Yan, C.Y. Soong, F. Chen, J. Power Sources 142 (2005) 125.
[28] S. Shimpalee, S. Greenway, J.W. Van Zee, J. Power Sources 160 (2006) 398.
[29] R.G. Reddy Kumar, J. Power Sources 155 (2006) 264.
[30] W.M. Yan, H.Y. Li, W.C. Tsai, J. Electrochem. Soc. 153 (2006) A1984.
[31] H.C. Liu, W.M. Yan, C.Y. Soong, F. Chen, H.S. Chu, J. Power Sources 158 (2006) 78.
[32] W.M. Yan, H.C. Liu, C.Y. Soong, F. Chen, C.H. Cheng, J. Power Sources 161 (2006) 907.
[33] S. Shimpalee, J.W. Van Zee, Int. J. Hydrogen Energy 32 (2007) 842.
[34] X.D. Wang, Y.Y. Duan, W.M. Yan, J. Power Sources 173 (2007) 210.
[35] H. Yang, T.S. Zhao, Electrochim. Acta 50 (2005) 3243.
[36] C. Xu, T.S. Zhao, Electrochem. Commun. 9 (2007) 497.
[37] X.D. Wang, Y.Y. Duan, W.M. Yan, X.F. Peng, J. Power Sources 175 (2008) 397.
[38] W.M. Yan, H.Y. Li, P.C. Chiu, X.D. Wang, J. Power Sources 178 (2008) 174.
[39] X.D. Wang, Y.Y. Duan, W.M. Yan, X.F. Peng, Electrochim. Acta 53 (2008) 5334.
[40] X.D. Wang, X.X. Zhang, W.M. Yan, D.J. Lee, A. Su, Int. J. Hydrogen Energy (2009), doi:10.1016/j.ijhydene.2008.12.049.
[41] T. Kanezaki, X. Li, J.J. Baschuk, J. Power Sources 162 (2006) 415.
[42] W.M. Yan, C.H. Yang, C.Y. Soong, F. Chen, S.C. Mei, J. Power Sources 160 (2006) 284.